

Bimetallic $\text{NH}_2\text{-MIL-101(Fe, Co)}$ as highly efficient photocatalyst for nitrogen fixation

Huifang Feng, Qiaozhen Xu, Tao Lv, Hong Liu^{*}

Department of Chemical Engineering, School of Environmental and Chemical Engineering, Shanghai University, 99 Shangda Road, Shanghai 200444, China

ARTICLE INFO

Keywords:

Metal organic frameworks
Bimetallic
Co doping
Photocatalytic N_2 fixation

ABSTRACT

Developing effective catalysts for N_2 photofixation at ambient conditions is highly desirable but still challenging. Herein, we reported a novel Co-doped $\text{NH}_2\text{-MIL-101(Fe)}$ (NM-Fe) bimetallic organic framework (BMOF) for visible-light-driven catalytic N_2 fixation. It was found that the doping of Co ions could effectively enhance light-harvesting, reduce the conduction band potential, suppress the recombination of photogenerated carriers, and promote the activation of N_2 . Consequently, the photocatalytic N_2 reduction efficiency of bimetallic $\text{NH}_2\text{-MIL-101(Fe, Co)}$ (NM-Fe-Co) was obviously boosted. The sample with the optical Co/Fe molar ratio of 0.15, namely NM-Fe-0.15Co, enabled an ammonia evolution rate up to $335.7 \mu\text{mol g}^{-1} \text{h}^{-1}$ without the aid of any sacrificial agents, a 4.4-fold increase over the monometallic NM-Fe baseline. Additionally, the bimetallic NM-Fe-Co displayed excellent stability. The possible reaction mechanism of nitrogen fixation over NM-Fe-Co was proposed based on in-situ infrared analysis. Our study demonstrates a promising strategy for designing potent MOF-based catalysts for N_2 photofixation.

1. Introduction

NH_3 is an important chemical feedstock and a clean energy carrier with high hydrogen content (17.6 wt%) [1–3]. At present, industrial-scale productions of ammonia are almost exclusively achieved via the Harber-Bosch process, in which N_2 is reduced to NH_3 through a dissociation pathway under a high temperature (400–500 °C) as well as an extremely high pressure (15–35 MPa) [1–3]. This process consumes a large amount of energy, usually in the form of burning non-renewable fossil fuels, generating a large amount of greenhouse gases. As a sustainable alternative, photocatalytic direct fixation of nitrogen is carried out through the association pathway, in which N_2 can be readily converted to NH_3 at ambient conditions, consuming only the energy-rich solar radiations [1–3]. Since the pioneering work on photocatalytic N_2 fixation using TiO_2 as a catalyst was reported by Schrauzer et al. in 1977 [4], various materials, including oxides [5,6], sulfides [7], oxyhalides [8,9] and $\text{g-C}_3\text{N}_4$ [10] have been investigated for N_2 reduction. However, most of them suffered from low efficiency due to the high energy barriers for N_2 adsorption and activation, low solar energy utilization, fast photogenerated electron-hole recombination, and other problems. Therefore, developing more efficient photocatalysts for N_2 reduction is highly demanded.

Metal-organic frameworks (MOFs), a class of emerging crystalline porous materials, have triggered great attention due to their potential application in drug delivery, sensing, catalysis, gas capture and separation [11,12]. The MOFs exhibit interesting characteristics such as high porosities, large surface areas, versatile metal nodes and tunable organic linkers, making them excellent candidates for photocatalysts. To date, various MOFs including $\text{NH}_2\text{-MIL-125(Ti)}$, UiO-66(Zr) , MIL-101(Fe) , MIL-53(Fe) and MOF-76(Ce) were applied to N_2 photofixation [13–17]. However, monometallic MOFs are inherently inefficient in terms of photocatalytic efficiency due to the excessive photo-carrier recombination, which can be remedied by a second metal in the skeleton node [18–22]. Constructing bimetallic nodes in MOFs not only provides additional active sites, but also inhibits the recombination of photoinduced carriers via the metal-to-metal charge transition (MMCT) process [18,20]. For instance, Shang et al. [19] synthesized bimetallic Al-PMOF (Fe) photocatalysts by introducing Fe into porphyrin-based Al-PMOF, which gave an ammonia yield of $127 \mu\text{g h}^{-1} \text{g}^{-1}$ under visible light, a 1.5-fold increase in nitrogen fixation rate when compared to the pristine Al-PMOF. An et al. [20] designed MOF-based photocatalysts U(Zr-Hf)-X ($\text{X} = \text{Cl, OH, SH}$) consisting of bimetallic Zr-Hf nodes. The best photocatalyst, U(0.5Hf)-2SH , enabled a N_2 fixation rate as high as $116.1 \mu\text{mol g}^{-1} \text{h}^{-1}$. Zhao et al. [21] prepared a series of bimetallic MOFs (BMOF

^{*} Corresponding author.

E-mail address: liuhong@shu.edu.cn (H. Liu).

<https://doi.org/10.1016/j.apcatb.2024.123949>

Received 26 January 2024; Received in revised form 4 March 2024; Accepted 10 March 2024

Available online 12 March 2024

0926-3373/© 2024 Elsevier B.V. All rights reserved.

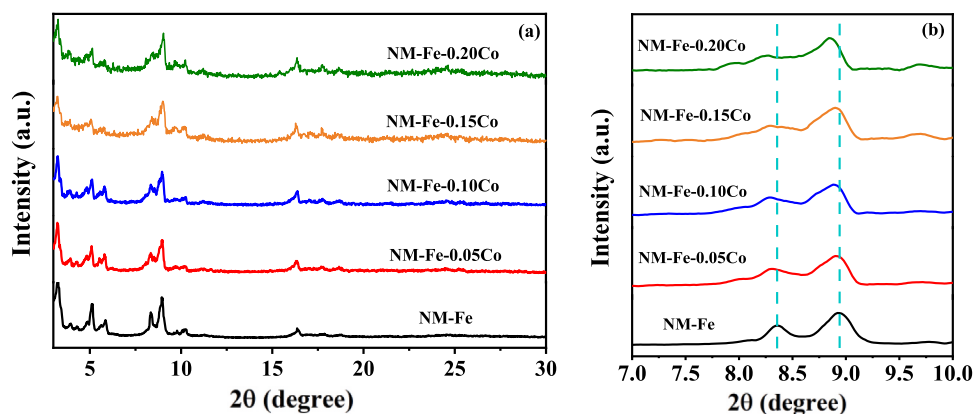


Fig. 1. (a) XRD patterns and (b) partially enlarged view of NM-Fe and NM-Fe-xCo ($x = 0.05, 0.10, 0.15$ and 0.20).

(Sr)-Fe) composed of Sr and Fe by a solvothermal method. Among all the prepared bimetallic MOFs, the BMOF(Sr)-0.2Fe photocatalyst exhibited the best photocatalytic nitrogen fixation performance ($780 \mu\text{mol g}^{-1} \text{h}^{-1}$). Zhang et al. [22] reported a bimetallic CeZr₅-MOF UiO-66 photocatalyst for photocatalytic N₂ reduction. The N₂ fixation rate of 15% Ce-UiO-66 reached $200.1 \mu\text{mol g}^{-1} \text{h}^{-1}$ under UV-vis light, also 105.9% higher than the monometallic baseline. Above researches demonstrate that the bimetallic synergistic effect in bimetallic MOFs can efficiently improve the photocatalytic N₂ fixation performance. Nevertheless, the application of bimetallic MOFs as photocatalysts for nitrogen fixation is still limited.

NH₂-MIL-101(Fe) (NM-Fe) is highly responsive to visible-light, non-toxic, outstandingly stable, and of low cost [23,24]. The similar radii and electron structures of Co and Fe atoms suggest the possibility of constructing isostructural frameworks via metallic substitution, leading to further performance gains.

Herein, we fabricated a novel bimetallic organic framework NH₂-MIL-101(Fe, Co) (NM-Fe-Co) using Fe and Co as metal nodes for visible-light-driven catalytic N₂ fixation. The doping of Co can effectively enhance light-harvesting, reduce the conduction band potential, inhibit the recombination of photogenerated carriers, and promote the activation of N₂. As a result, the photocatalytic N₂ fixation efficiency of NM-Fe-Co is vastly boosted. The maximum NH₃-production rate over NM-Fe-Co reaches $335.7 \mu\text{mol g}^{-1} \text{h}^{-1}$ without adding any sacrificial agent, 4.4 times that of NM-Fe. This value is higher than most MOF-based photocatalysts reported till date. Possible reaction mechanism of nitrogen fixation over NM-Fe-Co is further revealed by in-situ infrared analysis.

2. Experimental

2.1. Synthesis

NM-Fe-Co photocatalysts were synthesized by a solvothermal method. 0.27 g FeCl₃·6 H₂O (1 mmol), a certain amount of CoCl₂·6 H₂O, and 0.09 g 2-aminoterephthalic acid (NH₂-BDC, 0.5 mmol) were dispersed into 50 mL N,N-dimethylformamide (DMF) under magnetic stirring and sonicated for 1 h to obtain a dark green precursor solution. The obtained precursor was subsequently transferred to a polytetrafluoroethylene-lined autoclave (100 mL) and kept at 110 °C for 24 h. After cooling naturally to ambient temperature, the products were centrifuged and washed with DMF and ethanol. Lastly, the solid powders were collected after dried at 80 °C overnight. By varying the amount of CoCl₂·6 H₂O, the samples with Co/Fe molar ratios of 0.05, 0.10, 0.15 and 0.20 were obtained, which were noted as NM-Fe-xCo ($x = 0.05, 0.10, 0.15$ and 0.20 , respectively). Pristine NM-Fe was synthesized through the same procedure, but without adding CoCl₂·6 H₂O.

2.2. N₂ photoreduction

The N₂ photoreduction experiment was performed at ambient temperature and pressure. 30 mg of catalyst was dispersed in 100 mL of water in a quartz reactor. Subsequently, high purity N₂ was bubbled into the suspension at a flow rate of 100 mL min^{-1} under stirring for 30 min in the dark. The reactor was then irradiated by a 300 W Xenon lamp with a 420 nm filter. 5 mL of the reaction suspension was collected by a syringe every 1 h. The catalyst was filtered from the reaction solution using a disposable needle filter. The produced NH₃ amount was determined using the Nesslerization colorimetric method on a UV-Vis spectrophotometer based on the absorbance at 420 nm and calculated by the

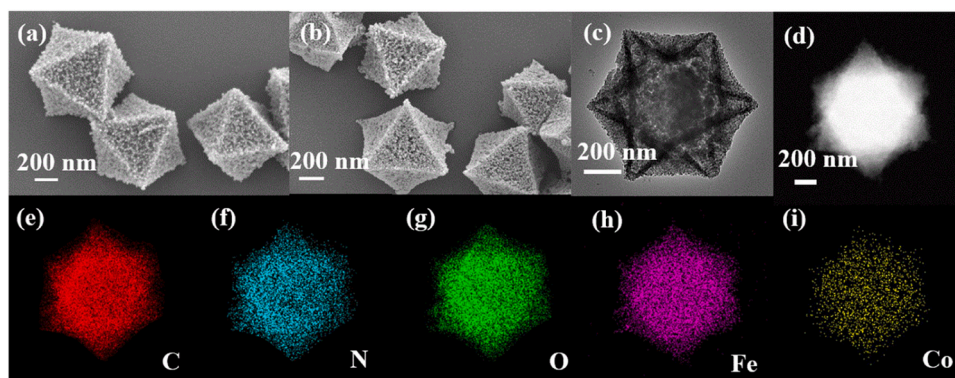


Fig. 2. SEM images of (a) NM-Fe and (b) NM-Fe-0.15Co; (c) TEM image and (d-i) element mapping of NM-Fe-0.15Co.

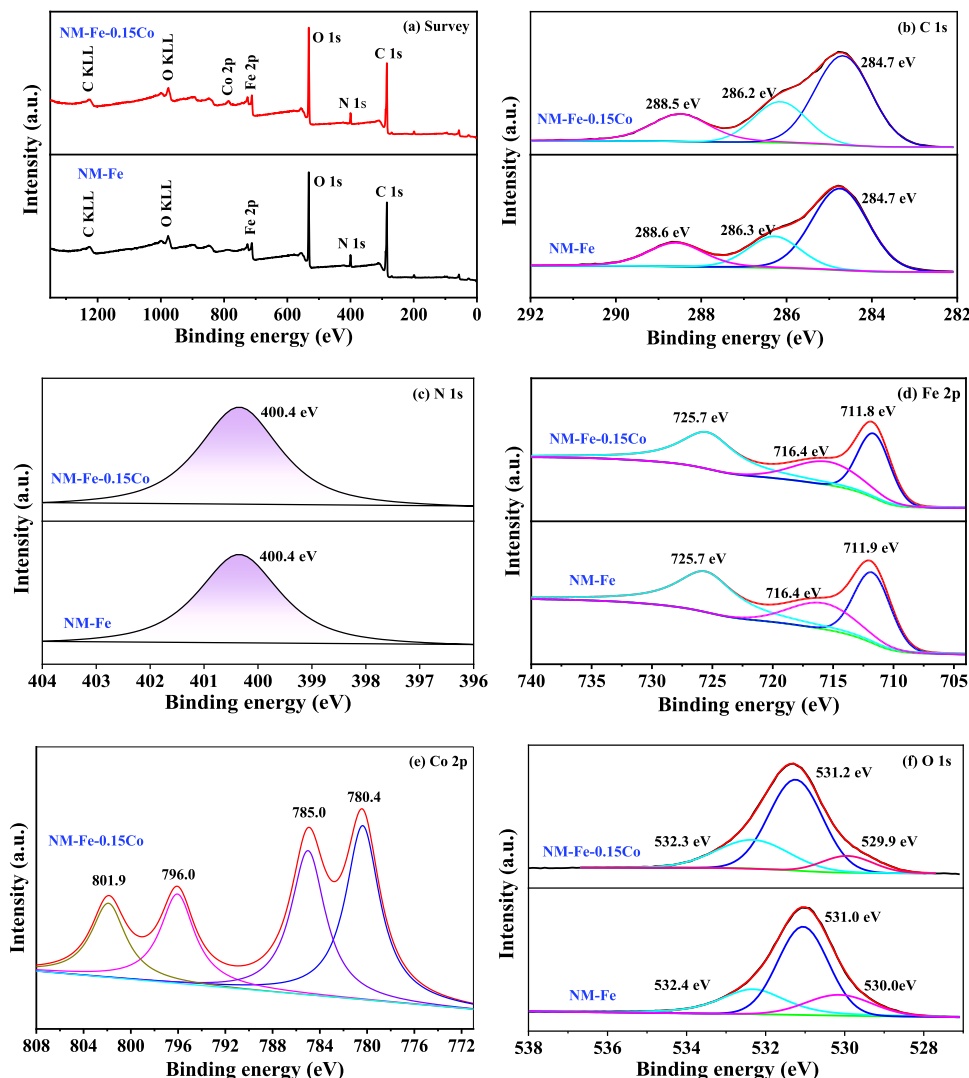


Fig. 3. XPS spectra of NM-Fe and NM-Fe-0.15Co: (a) Survey, (b) C 1 s, (c) N 1 s, (d) Fe 2p s, (e) Co 2p and (f) O 1 s.

calibration curve (Fig. S1).

The apparent quantum efficiency (AQE) for ammonia evolution was measured using 450 nm band-pass filters and calculated by the following equation:

$$\text{AQE} = \frac{3 \times \text{Number of evolved } \text{NH}_3 \text{ molecules}}{\text{Number of incident photons}} \times 100\%$$

$$= \frac{M \times N_A \times 3}{\frac{I \times A \times t}{h\nu}} \times 100\%$$

where M represents the molar number of generated ammonia molecules; N_A , I , A , t , h and ν are the Avogadro's constant, light intensity (17.0 mW cm^{-2}), light incident area (38.4 cm^2), light irradiation time, Planck constant and incident light frequency, respectively.

3. Results and discussion

3.1. Catalyst characterization

Fig. 1 shows the X-ray diffraction (XRD) patterns of NM-Fe and NM-Fe-xCo samples. The diffraction peaks of NM-Fe are consistent with those reported in the literatures [23–25], confirming the formation of the crystalline $\text{NH}_2\text{-MIL-101(Fe)}$ phase. The XRD patterns of NM-Fe-xCo are similar to that of NM-Fe, but the diffraction peak intensity decreases slightly after Co doping. The partially enlarged view (Fig. 1b) reveals

that the peaks in the range of $2\theta = 7^\circ \sim 10^\circ$ are shifted to a low angle with increasing Co doping, which is caused by the larger ionic radius of Co^{2+} (0.74 \AA) compared to Fe^{3+} (0.64 \AA). This result suggests that Co ions have been successfully inserted into the lattice of NM-Fe.

The morphologies of NM-Fe and NM-Fe-0.15Co were observed by scanning electron microscopy (SEM) and transmission electron microscopy (TEM). The NM-Fe sample has a regular octahedral morphology with a size of about 800 nm (Fig. 2a). The morphology and size of the NM-Fe-0.15Co sample remain unchanged after the doping of cobalt (Fig. 2b and c). The elemental mapping (Fig. 2d-i) of NM-Fe-0.15Co manifests that the Fe, Co, C, N and O elements are uniformly distributed in the sample.

Fourier transform infrared (FTIR) spectra of NM-Fe and NM-Fe-xCo samples are shown in Fig. S2. For NM-Fe, the bands at 769 , 1340 and 1659 cm^{-1} are assigned to C–H vibration, ν (C–N) and δ (N–H) [24,26,27], respectively. The bands in the region of $1578\text{--}1385 \text{ cm}^{-1}$ are due to the stretching of O–C–O [24,26,27], while the ones at 3361 and 3465 cm^{-1} correspond to the symmetrical and asymmetrical stretching vibrations of –NH_2 [24,26,27], respectively. The band at 575 cm^{-1} originates from the Fe–O vibration [24,26,27]. After the doping of Co, a new vibration peak of the Co–O bond appears at 523 cm^{-1} [28], and the signal of Co–O intensifies with the content of Co. This is a further indication of the successfulness of incorporating Co into NM-Fe.

X-ray photoelectron spectroscopy (XPS) was employed to examine to

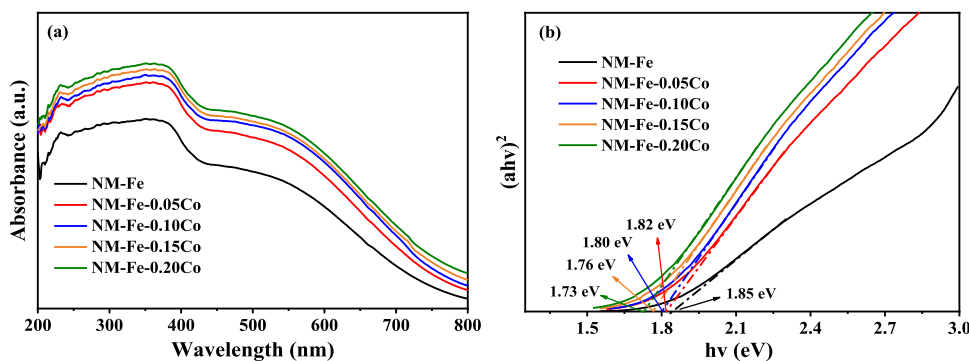


Fig. 4. (a) UV-vis DRS of NM-Fe and NM-Fe-xCo samples; (b) the corresponding plots of $(\alpha h\nu)^2$ vs. $(h\nu)$.

examine the surface chemical compositions and chemical state of as-synthesized photocatalysts. The overall XPS spectrum of NM-Fe-0.15Co shows the peaks corresponded to Fe, C, N, O and Co (Fig. 3a), implying the successful synthesis of bimetallic NM-Fe-Co. The C 1s spectrum of NM-Fe-0.15Co exhibits three peaks located at 284.7, 286.2 and 288.5 eV (Fig. 3b), which can be assigned to the C-C bond, C-N bond and carboxylate group (O-C=O) [23,24,29], respectively. The peak at 400.4 eV in the N 1s spectrum of NM-Fe-0.15Co (Fig. 3c) corresponds to the C-N bond of the NH₂-BDC ligand [23,24]. There are three prominent peaks at 711.8 (Fe 2p_{3/2}), 725.7 (Fe 2p_{1/2}) and 716.4 eV (satellite peak of Fe 2p_{3/2}) in Fe 2p spectrum of NM-Fe-0.15Co (Fig. 3d), indicating the presence of Fe³⁺ [23,24,29]. The Co 2p spectrum of NM-Fe-0.15Co (Fig. 3e) presents two prominent peaks at 780.4 (Co 2p_{3/2}) and 796.0 (Co 2p_{1/2}) eV, along with two satellite peaks (785.0 and 801.9 eV), suggesting the presence of the element Co in the form of Co²⁺ [30,31]. The peaks at 529.9, 531.2 and 532.3 eV in the O 1s spectrum of NM-Fe-0.15Co (Fig. 3f) belong to the Fe-O bond, the carbonyl O=C group and the surface oxygen vacancies (OVs) [14,23,24,32], respectively. Compared to NM-Fe, the XPS peak area of OVs becomes larger for NM-Fe-0.15Co, which indicates that the concentration of OVs in NM-Fe-0.15Co is higher than that in NM-Fe. The presence and

increase of OVs can be further probed by the ESR measurements. As illustrated in Fig. S3, both samples show obvious oxygen vacancy signals ($g=2.003$), while the oxygen vacancy signal of NM-Fe-0.15Co is stronger, demonstrating that Co doping can promote the formation of oxygen vacancies. The higher OVs is more favorable to the chemisorption and activation of N₂ molecules [14,33,34].

The optical properties of NM-Fe and NM-Fe-xCo were evaluated using UV-vis diffuse reflectance spectroscopy (DRS). As presented in Fig. 4a, NM-Fe has a broad optical response from 200 to 800 nm. Compared to NM-Fe, the light absorption intensity of NM-Fe-xCo is enhanced, and the absorption edge is significantly red-shifted, which may be due to the synergistic effect between Fe and Co [18]. The band gap values (E_g) of the samples can be estimated by the Tauc equation: $(\alpha h\nu)^2 = k(h\nu - E_g)$. As shown in Fig. 4b, the E_g values of NM-Fe, NM-Fe-0.05Co, NM-Fe-0.10Co, NM-Fe-0.15Co and NM-Fe-0.20Co are about 1.85, 1.82, 1.80, 1.76 and 1.73 eV, respectively.

The flat-band potentials (E_{fb}) of NM-Fe and NM-Fe-0.15Co can be obtained from the Mott-Schottky (M-S) plots. As exhibited in Fig. S4, both materials are n-type semiconductors according to their positive slopes in M-S curves [23,32]. The E_{fb} of NM-Fe and NM-Fe-0.15Co are -0.63 V vs. Ag/AgCl (-0.43 V vs. NHE) and -0.90 V vs. Ag/AgCl

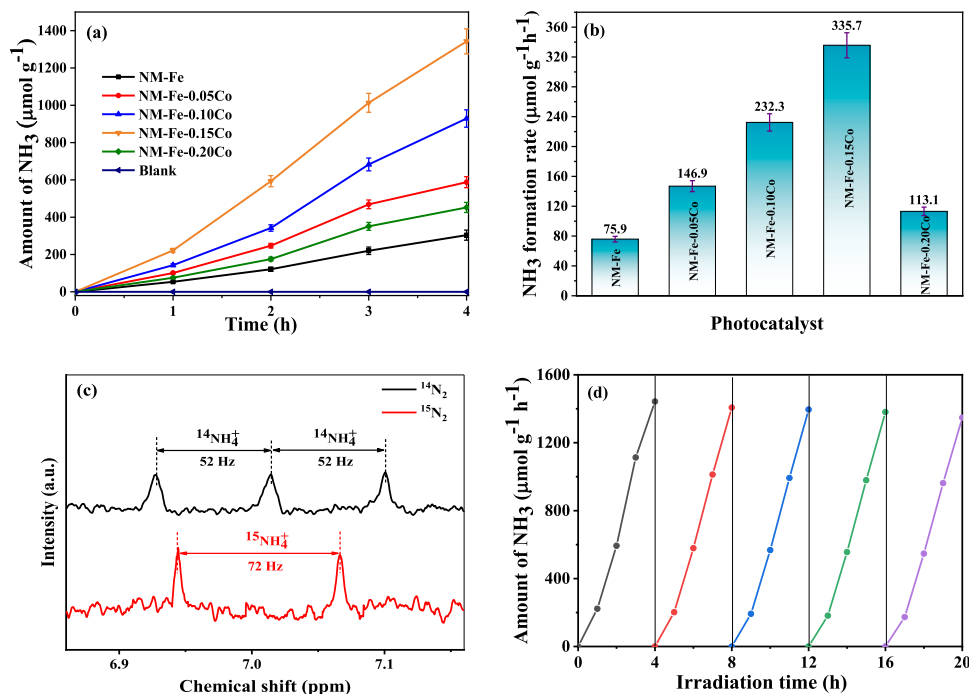


Fig. 5. (a-b) NH₃ evolution rates over different catalysts; (c) ¹H NMR spectra of ¹⁴NH₄⁺ and ¹⁵NH₄⁺ formed via the N₂ photofixation reaction over NM-Fe-0.15Co in ¹⁴N₂ and ¹⁵N₂ atmosphere; (d) Recyclability test of NM-Fe-0.15Co.

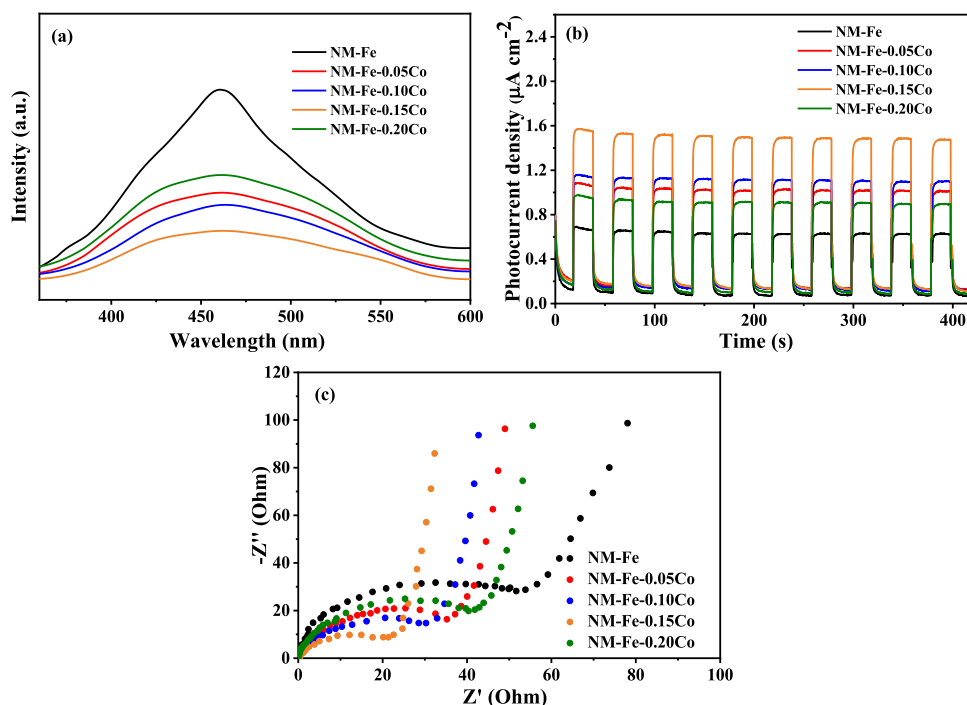


Fig. 6. (a) PL spectra, (b) photocurrents and (c) EIS of NM-Fe and NM-Fe-xCo.

(-0.70 V vs. NHE), respectively. Given that the conduction band (CB) potential of an n-type semiconductor is usually 0.1 V lower than its flat band potential [35,36], the CB potentials of NM-Fe and NM-Fe-0.15Co are found to be -0.53 and -0.80 eV, respectively, which can satisfy the reduction potential of nitrogen fixation (-0.28 eV) from the thermodynamic point of view. In addition, the CB potential of NM-Fe-0.15Co is lower than that of NM-Fe, indicating that NM-Fe-0.15Co has a stronger reduction capacity for nitrogen fixation.

The porosity and specific surface area of NM-Fe and NM-Fe-xCo photocatalysts were measured by the N_2 adsorption method. As illustrated in Fig. S5a, the adsorption isotherms of NM-Fe and NM-Fe-xCo are type-I isotherms, indicating that these samples are microporous materials [37]. In addition, NM-Fe-0.15Co and NM-Fe-0.20Co show an H3-hysteresis loop at high P/P_0 , indicating that some mesopores are present in the samples. The pore size distributions (Fig. S5b-c) reveal three major pores at 0.46, 0.52 and 1.88 nm in NM-Fe, while there is consistency in the pore size distribution of NM-Fe-xCo and NM-Fe. As shown in Table S1, the specific surface areas of NM-Fe, NM-Fe-0.05Co, NM-Fe-0.10Co, NM-Fe-0.15Co and NM-Fe-0.20Co are 240.0, 259.3, 285.9, 326.4 and 371.9 $m^2 g^{-1}$, respectively. The specific surface areas of bimetallic NM-Fe-xCo are larger than that of NM-Fe. The larger specific surface areas of bimetallic MOFs will provide more active sites, which is beneficial for enhancing photocatalytic nitrogen fixation.

3.2. Photocatalytic N_2 fixation performance

The photocatalytic N_2 fixation experiments were conducted in pure water in absence of sacrificial agent. As depicted in Fig. 5a and b, pristine NM-Fe has a weak N_2 fixation capacity with an NH_3 -production rate of 75.9 $\mu mol g^{-1} h^{-1}$. As expected, the production of NH_3 is greatly improved by the doping of cobalt ions. As the Co/Fe molar ratio increases, the photocatalytic NH_3 -production rate of NM-Fe-xCo increases at first and then decreases. Among all the as-prepared samples, NM-Fe-0.15Co exhibits the highest NH_3 -production rate (335.7 $\mu mol g^{-1} h^{-1}$), about 4.4 times of pristine NM-Fe, which is also superior to the most of MOF-based photocatalysts (Table S2). The AQE of NM-Fe-0.15Co was calculated to be 0.10% at 450 nm. Furthermore, control tests were carried out, and no ammonia was produced in the absence of

photocatalyst, light and N_2 (using Ar as a replacement). To confirm the origin of the produced NH_3 , an isotope labeling experiment was performed using $^{14}N_2$ and $^{15}N_2$ as the N_2 sources. As revealed in Fig. 5c, the triplet and doublet peaks corresponding to $^{14}NH_4^+$ and $^{15}NH_4^+$ were observed in the 1H NMR spectra when $^{14}N_2$ and $^{15}N_2$ were used as nitrogen sources, respectively. This result verifies that the generated NH_3 originated from N_2 gas.

To monitor the generation of O_2 during the photocatalytic N_2 fixation, a closed experimental setup was designed (Fig. S6a). As shown in Fig. S6b and c, the O_2 produced due to the oxidation of water ($H_2O + 2 h^+ \rightarrow 1/2 O_2 + 2 H^+$) is demonstrated, and the amount of generated O_2 is increasing with the extension of the light irradiation time. Meanwhile, the relative concentration of N_2 decreases gradually because of the conversion of N_2 into NH_3 ($N_2 + 6 e^- + 6 H^+ \rightarrow 2 NH_3$).

To verify the stability of NM-Fe-Co, we conducted cycling experiments on NM-Fe-0.15Co. The photocatalytic N_2 fixation activity of NM-Fe-0.15Co exhibits a slight decrease during the cycling rounds (Fig. 5d), which may be caused by the loss of catalyst during the recycling runs. Additionally, the crystal structure (Fig. S7a) and morphology (Fig. S7b) of the used photocatalyst show no significant change. The above results indicate that the NM-Fe-0.15Co photocatalyst has good stability in the photocatalytic N_2 fixation process.

3.3. Photocatalytic mechanism

To explicate the intrinsic mechanism of high activity of bimetallic NM-Fe-xCo, photoluminescence (PL) spectra, electrochemical impedance spectra (EIS) and transient photocurrent response were determined. As shown in Fig. 6a, NM-Fe has a strong PL peak at 460 nm, indicating its high electron-hole recombination rate. The PL intensities of all NM-Fe-xCo samples are weaker than that of NM-Fe, indicating that the doping of Co effectively suppressed the recombination of photoexcited carriers in NM-Fe-xCo. The order of PL intensity is NM-Fe > NM-Fe-0.20Co > NM-Fe-0.05Co > NM-Fe-0.10Co > NM-Fe-0.15Co, corresponding to the order of their nitrogen fixation activities. As shown in Fig. 6b, the bimetallic NM-Fe-xCo samples exhibit higher photocurrents than NM-Fe, suggesting enhanced charge transfer efficiencies among the NM-Fe-xCo samples. The arc radius of the NM-Fe-xCo samples is smaller

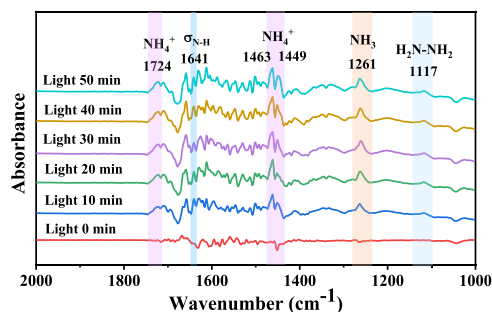
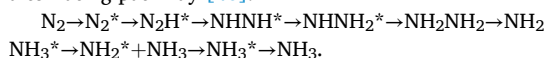


Fig. 7. In-situ FTIR spectra of NM-Fe-0.15Co.

than that of NM-Fe (Fig. 6c), indicating the NM-Fe-xCo samples have lower charge transfer resistance. These results demonstrate that the doping of Co can effectively improve the migration and separation of photoexcited carriers, which is conducive to the improvement of photocatalytic nitrogen fixation. Moreover, compared with NM-Fe, bimetallic NM-Fe-Co possesses more oxygen vacancies, which is beneficial to the adsorption and activation of N_2 [14,33,34]. The UV-vis DRS and Mott-Schottky results reveal that the light absorption of NM-Fe-Co is elevated, and the CB potential becomes more negative, which is also favorable for photocatalytic nitrogen fixation.

The activation and reduction reaction pathways of N_2 over NM-Fe-0.15Co catalyst were investigated by in-situ FTIR, and the results are presented in Fig. 7. Upon light irradiation, new IR peaks emerge at 1724, 1641, 1463, 1449, 1261 and 1117 cm^{-1} . Among them, the peak at 1641 cm^{-1} originates from the bending vibration of N-H (σ_{N-H}) [21,37,38]. The peak at 1117 cm^{-1} is attributed to the stretching vibration of H_2N-NH_2 [21,38,39]. The peaks at 1724, 1463 and 1449 cm^{-1} are associated with the absorption of NH_4^+ [21,38,39]. The peak at 1261 cm^{-1} belongs to the absorption of NH_3 [21,38,39]. The intensities of the absorption peaks corresponding to the above intermediates and products are all enhanced with increasing illumination time. The appearance of the H_2N-NH_2 intermediate indicates that the N_2 adsorbed on the surface of the NM-Fe-0.15Co is reduced to NH_3 via the associative alternating pathway [40]:



4. Conclusions

In this work, bimetallic NM-Fe-Co photocatalysts with different Co/Fe ratios were prepared by a solvothermal method and used for visible-light-driven photocatalytic N_2 fixation. The optimal catalytic activity was achieved when the molar ratio of Co/Fe was 0.15, yielding 335.7 $\mu mol\ g^{-1}\ h^{-1}$ of ammonia in absence of sacrificial agents, which was 4.4 times that of NM-Fe. In addition, the NM-Fe-Co photocatalyst had good photochemical stability. The improved activity of the bimetallic NM-Fe-Co stemmed from the synergetic effect of the enhanced light absorption, improved charge carrier separation, more negative conduction band, and more efficient N_2 activation. The in-situ FTIR results indicate that H_2N-NH_2 is an intermediate product of the N_2 reduction process, and the N_2 adsorbed on the NM-Fe-Co photocatalyst is reduced to NH_3 by an associative alternating pathway.

CRediT authorship contribution statement

Huifang Feng: Writing – original draft, Investigation. **Qiaozhen Xu:** Investigation. **Tao Lv:** Validation. **Hong Liu:** Writing – review & editing, Supervision, Funding acquisition, Conceptualization.

Declaration of Competing Interest

The authors declare that they have no known competing financial

interests or personal relationships that could have appeared to influence the work reported in this paper.

Data Availability

Data will be made available on request.

Acknowledgments

This work was supported by the Shanghai Municipal People's Government (21DZ1209200).

Appendix A. Supporting information

Supplementary data associated with this article can be found in the online version at doi:10.1016/j.apcatb.2024.123949.

References

- [1] R. Shi, Y. Zhao, G.I.N. Waterhouse, S. Zhang, T. Zhang, Defect engineering in photocatalytic nitrogen fixation, *ACS Catal.* 9 (2019) 9739–9750, <https://doi.org/10.1021/acscatal.9b03246>.
- [2] L. Wang, W. Wu, K. Liang, X. Yu, Advanced strategies for improving the photocatalytic nitrogen fixation performance: a short review, *Energy Fuels* 36 (2022) 11278–11291, <https://doi.org/10.1021/acs.energyfuels.2c01083>.
- [3] J. Lee, L.L. Tan, S.P. Chai, Heterojunction photocatalysts for artificial nitrogen fixation: fundamentals, latest advances and future perspectives, *Nanoscale* 13 (2021) 7011–7033, <https://doi.org/10.1039/D1NR00783A>.
- [4] G.N. Schrauzer, T.D. Guth, Photolysis of water and photoreduction of nitrogen on titanium dioxide, *J. Am. Chem. Soc.* 99 (1977) 7189–7193.
- [5] H. Li, M. Xia, B. Chong, H. Xiao, B. Zhang, B. Lin, B. Yang, G. Yang, Boosting photocatalytic nitrogen fixation via constructing low-oxidation-state active sites in the nanoconfined spinel iron cobalt oxide, *ACS Catal.* 12 (2022) 10361–10372, <https://doi.org/10.1021/acscatal.2c02282>.
- [6] J. Ye, J. Xu, C. Li, D. Tian, X. Zhao, Q. Wang, W. Lv, J. Wang, H. Xie, Y. Li, Z. Liu, Y. Fu, Novel N-black $In_2O_3-x/InVO_4$ heterojunction for efficient photocatalytic fixation: synergistic effect of exposed (321) facet and oxygen vacancy, *J. Mater. Chem.* 9 (2021) 24600–24612, <https://doi.org/10.1039/d1ta08257d>.
- [7] G. Swain, S. Sultana, K. Parida, Constructing a novel surfactant-free MoS_2 nanosheet modified $MgIn_2S_4$ marigold microflower: an efficient visible-light driven 2D–2D p–n heterojunction photocatalyst toward HER and pH regulated NRR, *ACS Sustain. Chem. Eng.* (12) (2020) 4848–4862, <https://doi.org/10.1021/acssuschemeng.9b07821>.
- [8] Y. Shiraishi, M. Hashimoto, K. Chishiro, K. Moriyama, S. Tanaka, T. Hirai, Photocatalytic dinitrogen fixation with water on bismuth oxychloride in chloride solutions for solar-to-chemical energy conversion, *J. Am. Chem. Soc.* 142 (2020) 7574–7583, <https://doi.org/10.1021/jacs.0c01683>.
- [9] P. Li, Z. Zhou, Q. Wang, M. Guo, S. Chen, J. Low, R. Long, W. Liu, P. Ding, Y. Wu, Y. Xiong, Visible-light-driven nitrogen fixation catalyzed by Bi_5O_7Br nanostructures: enhanced performance by oxygen vacancies, *J. Am. Chem. Soc.* 142 (2020) 12430–12439, <https://doi.org/10.1021/jacs.0c05097>.
- [10] L. Zhang, S. Hou, T. Wang, S. Liu, X. Gao, C. Wang, G. Wang, Recent advances in application of graphitic carbon nitride-based catalysts for photocatalytic nitrogen fixation, *Small* 18 (2022) 2202252, <https://doi.org/10.1002/sml.202202252>.
- [11] R. Li, W. Zhang, K. Zhou, Metal-organic-framework-based catalysts for photoreduction of CO_2 , *Adv. Mater.* 30 (2018) 1705512, <https://doi.org/10.1002/adma.201705512>.
- [12] K. Hu, Z. Huang, L. Zeng, Z. Zhang, L. Mei, Z. Chai, W. Shi, Recent advances in MOF-based materials for photocatalytic nitrogen fixation, *Eur. J. Inorg. Chem.* (2021) 1–16, <https://doi.org/10.1002/ejic.202100748>.
- [13] C. Zhang, Y. Xu, C. Lv, X. Zhou, Y. Wang, W. Xing, Q. Meng, Y. Kong, G. Chen, Mimicking π backdonation in Ce-MOFs for solar-driven ammonia synthesis, *ACS Appl. Mater. Interfaces* 11 (2019) 29917–29923, <https://doi.org/10.1021/acsaami.9b08682>.
- [14] Z. Zhao, D. Yang, H. Ren, K. An, Y. Chen, Z. Zhou, W. Wang, Zh Jiang, Nitrogenase-inspired mixed-valence MIL-53(Fe^{II}/Fe^{III}) for photocatalytic nitrogen fixation, *Chem. Eng. J.* 400 (2020) 125929, <https://doi.org/10.1016/j.cej.2020.125929>.
- [15] G. Li, F. Li, J. Liu, C. Fan, Fe-based MOFs for photocatalytic N_2 reduction: Key role of transition metal iron in nitrogen activation, *J. Solid State Chem.* 285 (2020) 121245, <https://doi.org/10.1016/j.jssc.2020.121245>.
- [16] H. Huang, X.S. Wang, D. Philo, F. Ichihara, H. Song, Y. Li, D. Li, T. Qiu, S. Wang, J. Ye, Toward visible-light-assisted photocatalytic nitrogen fixation: a titanium metal organic framework with functionalized ligands, *Appl. Catal. B: Environ.* 267 (2020) 118686, <https://doi.org/10.1016/j.apcatb.2020.118686>.
- [17] W. Gao, X. Li, X. Zhang, S. Su, S. Luo, R. Huang, Y. Jing, M. Luo, Photocatalytic nitrogen fixation of metal-organic frameworks (MOFs) excited by ultraviolet light: insights into the nitrogen fixation mechanism of missing metal cluster or linker defects, *Nanoscale* 13 (2021) 7801–7809, <https://doi.org/10.1039/d1nr00697e>.

- [18] L. Chen, H.F. Wang, C. Li, Q. Xu, Bimetallic metal-organic frameworks and their derivatives, *Chem. Sci.* 11 (2020) 5369–5403, <https://doi.org/10.1039/d0sc01432j>.
- [19] S. Shang, W. Xiong, C. Yang, B. Johannessen, R. Liu, H.Y. Hsu, Q. Gu, M.K. H. Leung, J. Shang, Atomically dispersed iron metal site in a porphyrin-based metal-organic framework for photocatalytic nitrogen fixation, *ACS Nano* 15 (2021) 9670–9678, <https://doi.org/10.1021/acsnano.0c10947>.
- [20] K. An, H. Ren, D. Yang, Z. Zhao, Y. Gao, Y. Chen, J. Tan, W. Wang, Z. Jiang, Nitrogenase-inspired bimetallic metal organic frameworks for visible-light-driven nitrogen fixation, *Appl. Catal. B: Environ.* 292 (2021) 120167, <https://doi.org/10.1016/j.apcatb.2021.120167>.
- [21] Z. Zhao, H. Ren, D. Yang, Y. Han, J. Shi, K. An, Y. Chen, Y. Shi, W. Wang, J. Tan, X. Xin, Y. Zhang, Z. Jiang, Boosting nitrogen activation via bimetallic organic frameworks for photocatalytic ammonia synthesis, *ACS Catal.* 11 (15) (2021) 9986–9995, <https://doi.org/10.1021/acscatal.1c02465>.
- [22] X. Zhang, X. Li, W. Gao, S. Luo, S. Su, R. Huang, M. Luo, Bimetallic CeZr₅-UiO-66 as a highly efficient photocatalyst for the nitrogen reduction reaction, *Sustain. Energy Fuels* 5 (2021) 4053, <https://doi.org/10.1039/d1se00658d>.
- [23] H. Feng, Y. Sun, Q. Xu, H. Liu, Construction of NH₂-MIL-101(Fe)/Bi₂MoO₆ S-scheme heterojunction for efficient and selective photocatalytic CO₂ conversion to CO, *Appl. Catal. A: Gen.* 664 (2023) 119350, <https://doi.org/10.1016/j.apcata.2023.119350>.
- [24] Q. Xu, Y. Sun, T. Lv, H. Liu, Selective CO₂ photoreduction into CO over Ti₃C₂ quantum dots decorated NH₂-MIL-101(Fe) heterostructures, *J. Alloy. Compd.* 954 (2023) 170088, <https://doi.org/10.1016/j.jallcom.2023.170088>.
- [25] X.Y. Dao, X.F. Xie, J.H. Guo, X.Y. Zhang, Y.S. Kang, W.Y. Sun, Boosting photocatalytic CO₂ reduction efficiency by heterostructures of NH₂-MIL-101(Fe)/g-C₃N₄, *ACS Appl. Energy Mater.* 3 (2020) 3946–3954, <https://doi.org/10.1021/acsaem.0c00352>.
- [26] H. Shi, C. Li, L. Wang, W. Wang, X. Meng, Selective reduction of nitrate into N₂ by novel Z-scheme NH₂-MIL-101(Fe)/BiVO₄ heterojunction with enhanced photocatalytic activity, *J. Hazard. Mater.* 424 (2022) 127711 <https://doi.org/10.1016/j.jhazmat.2021.127711>.
- [27] Y. Wang, H. Fang, S. Liang, X. Sheng, Y. Huang, Y. Zhang, Y. Zhou, Functionalized ⁹D-³D heterostructure with ameliorated charge separation kinetics enables efficient photocatalytic hydrogen evolution, *Appl. Surf. Sci.* 606 (2022) 154872, <https://doi.org/10.1016/j.apsusc.2022.154872>.
- [28] S. Sivakumar, L.N. Prabu, Enhancement in electrochemical behavior of cobalt doped α-MnO₂ nanoparticles, *Inorg. Chem. Commun.* 147 (2023) 110247, <https://doi.org/10.1016/j.inoche.2022.110247>.
- [29] S. Li, C. Wang, Y. Liu, Y. Liu, M. Cai, W. Zhao, X. Duan, S-scheme MIL-101(Fe) octahedrons modified Bi₂WO₆ microspheres for photocatalytic decontamination of Cr(VI) and tetracycline hydrochloride: synergistic insights, reaction pathways, and toxicity analysis, *Chem. Eng. J.* 455 (2023) 140943, <https://doi.org/10.1016/j.cej.2022.140943>.
- [30] Y. Sun, M. Xie, H. Feng, H. Liu, Efficient visible-light-driven photocatalytic hydrogen generation over 2D/2D Co-ZIF-9/Ti₃C₂ hybrids, *ChemPlusChem* 87 (2022) e202100553, <https://doi.org/10.1002/cplu.202100553>.
- [31] S. Zhao, J. Xu, M. Mao, L. Li, X. Li, Protonated g-C₃N₄ cooperated with Co-MOF doped with Sm to construct 2D/2D heterojunction for integrated dye-sensitized photocatalytic H₂ evolution, *J. Colloid Interface Sci.* 583 (2021) 435–447, <https://doi.org/10.1016/j.jcis.2020.09.063>.
- [32] J. Meng, Q. Chen, J. Lu, H. Liu, Z-scheme photocatalytic CO₂ reduction on a heterostructure of oxygen-defective ZnO/reduced graphene oxide/UiO-66-NH₂ under visible light, *ACS Appl. Mater. Interfaces* 11 (2019) 550–562, <https://doi.org/10.1021/acsami.8b14282>.
- [33] M. Cheng, C. Xiao, Y. Xie, Photocatalytic nitrogen fixation: the role of defects in photocatalysts, *J. Mater. Chem. A* 7 (2019) 19616–19633, <https://doi.org/10.1039/c9ta06435d>.
- [34] Y. Chen, Q. Sun, X. Tu, L. Chen, W. Han, L. Zhang, X. Duan, M. Liu, H. Zheng, Bio-inspired citric acid-based bimetallic photocatalyst for nitrogen fixation from air under ambient conditions, *J. Clean. Prod.* 392 (2023) 136314, <https://doi.org/10.1016/j.jclepro.2023.136314>.
- [35] S. Saha, G. Das, J. Thote, R. Banerjee, Photocatalytic metal-organic framework from CdS quantum dot incubated luminescent metallohydrogel, *J. Am. Chem. Soc.* 136 (2014) 14845, <https://doi.org/10.1021/ja509019k>.
- [36] C.W. Zhao, Y.A. Li, X.R. Wang, G.J. Chen, Q.K. Liu, J.P. Ma, Y.B. Dong, Fabrication of Cd(II)-MOF-based ternary photocatalytic composite materials for H₂ production via a gel-to-crystal approach, *Chem. Commun.* 51 (2015) 15906, <https://doi.org/10.1039/c5cc06291h>.
- [37] L. Wang, P. Jin, J. Huang, H. She, Q. Wang, Integration of copper(II)-porphyrin zirconium metal-organic framework and titanium dioxide to construct Z-scheme system for highly improved photocatalytic CO₂ reduction, *ACS Sustain. Chem. Eng.* 7 (2019) 15660–15670, <https://doi.org/10.1021/acssuschemeng.9b03773>.
- [38] T. He, Z. Zhao, R. Liu, X. Liu, B. Ni, Y. Wei, Y. Wu, W. Yuan, H. Peng, Z. Jiang, Y. Zhao, Porphyrin-based covalent organic frameworks anchoring Au single atoms for photocatalytic nitrogen fixation, *J. Am. Chem. Soc.* 145 (2023) 6057–6066, <https://doi.org/10.1021/jacs.2c10233>.
- [39] G. Wang, T. Huo, Q. Deng, F. Yu, Y. Xia, H. Li, W. Hou, Surface-layer bromine doping enhanced generation of surface oxygen vacancies in bismuth molybdate for efficient photocatalytic nitrogen fixation, *Appl. Catal. B: Environ.* 310 (2022) 121319, <https://doi.org/10.1016/j.apcatb.2022.121319>.
- [40] H. Li, J. Wang, Z. Ruan, P. Nan, B. Ge, M. Cheng, L. Yang, X. Li, Q. Liu, B. Pan, Q. Zhang, C. Xiao, Y. Xie, Electron transfer bridge inducing polarization of nitrogen molecules for enhanced photocatalytic nitrogen fixation, *Mater. Horiz.* 10 (2023) 5053–5059, <https://doi.org/10.1039/d3mh01041d>.